Geothermal Energy

RESEARCH

Open Access

Geothermal resources assessment using temperature–depth relationships in the fault-controlled hydrothermal system of Aristino-Traianoupolis area, Northern Greece

P. Dalampakis[1*], M. Papachristou[2] and P. Neofotistos[2]

*Correspondence: p.dalampakis@swri.gr

[1] Soil and Water Resources Institute, Hellenic Agricultural Organization DIMITRA, 57400 Sindos, Greece
[2] School of Geology, Aristotle University of Thessaloniki, 54124 Thessaloniki, Greece

Abstract

Aristino-Traianoupolis area hosts one of the most significant water-dominated low-temperature geothermal fields in Greece. It is located on the southwestern uplifted margin of the Tertiary Evros Delta molassic basin, 10 km east of the town of Alexandroupolis (Thrace, NE Greece). The upper hydrothermal system of the Aristino Geothermal Field (AGF), one of the most promising in continental Greece, contains fluids with temperatures ranging from 51 to 99 °C, within a series of overlapping aquifers at very low depths (100–430 m). The main geothermal anomaly for temperatures higher than 90 °C covers an area of 6 km^2, to a maximum prospected depth of 500 m below ground surface. The scattered regional anomaly exceeds 50 km^2 and is characterized by excessively high and abruptly changing thermal gradient (42 to 450 °C/km) and heat flow (80–800 mW/m^2), that are both typical of a fault-controlled hydrothermal system. Since 1993, the AGF has undergone non-systematic geothermal investigation, with emphasis on low-depth (100–500 m) drilling. This paper provides, for the first time, a synthetic and detailed evaluation of all available temperature data gathered in the last 25 years. The steady-state temperature logs reveal the dominant role of conduction for the upper geothermal system, accompanied, in most cases, by rapidly changing and abnormally high thermal gradients (100–450 °C/km), triggered, most probably, by a deeper system of higher temperature. This hypothesis is also supported by the applied chemical geothermometers, which suggest initial fluid temperatures at 140–150 °C, the hydrochemical characteristics of the fluids hosted in the deeper and most promising investigated reservoir (ignimbrite) of the upper system, and the extrapolated temperatures from the conductive temperature–depth profiles. The lower widespread medium enthalpy hydrothermal system should extend at depths 500–1000 m within volcanics and the expected Eocene limestones and basal clastic series of the Tertiary sequence that have filled the basin. Nevertheless, these assumptions need to be verified by appropriate investigations and new drillings at depths greater than 600–700 m, which would confirm the presence of a productive medium enthalpy reservoir.

Keywords: Low enthalpy system, Tectonics, Temperature logs, Geothermal Gradient, Heat Flow, Conceptual Model

Introduction

Northeastern Greece has been subjected, since the early 80s, to systematic geothermal exploration, which identified many low enthalpy geothermal areas with fluid temperature up to 92.5 °C (Kolios et al. 2007). These hydrothermal systems are located at relatively low depths (< 600 m) within the Tertiary post-orogenic sedimentary basins of eastern Macedonia and Thrace (Fig. 1). Their formation was favored by the extensional tectonics and crustal thinning, followed by abnormal regional heat flow increase, and shifting of isotherms toward the surface, a procedure that was intensified by the synchronous emplacement of magmatic intrusions (Tertiary plutonic and volcanic rocks). These basins remain thermally active until today (Kolios et al. 2007).

One of the most prominent geothermal areas in northeastern Greece is located in the southwestern margin of the Thrace basin (Fig. 2), primarily filled with Paleogene molasse-type sediments (Kilias et al. 2015), in the wider area of Aristino (Aristino Geothermal Field––AGF). The presence of the fault-controlled discharging area of the Traianoupolis thermal spring, the significant and widespread hydrothermal alterations, and the occurrence of intersected deep strike-slip and normal faults were the sole surficial indications for the presence of an active hydrothermal system.

The present study is based on data acquired from twenty (20) wells that were drilled in this area during the period 1988–2016 (Fig. 3). Except from AA6, which was drilled in 2016, all other wells were constructed 17 to 33 years ago.

The already investigated and explored hot aquifers are regarded as the *upper* geothermal system of the region, which has been developed inside various lithological complexes (volcano-sedimentary and volcanic formations), bounded by a major

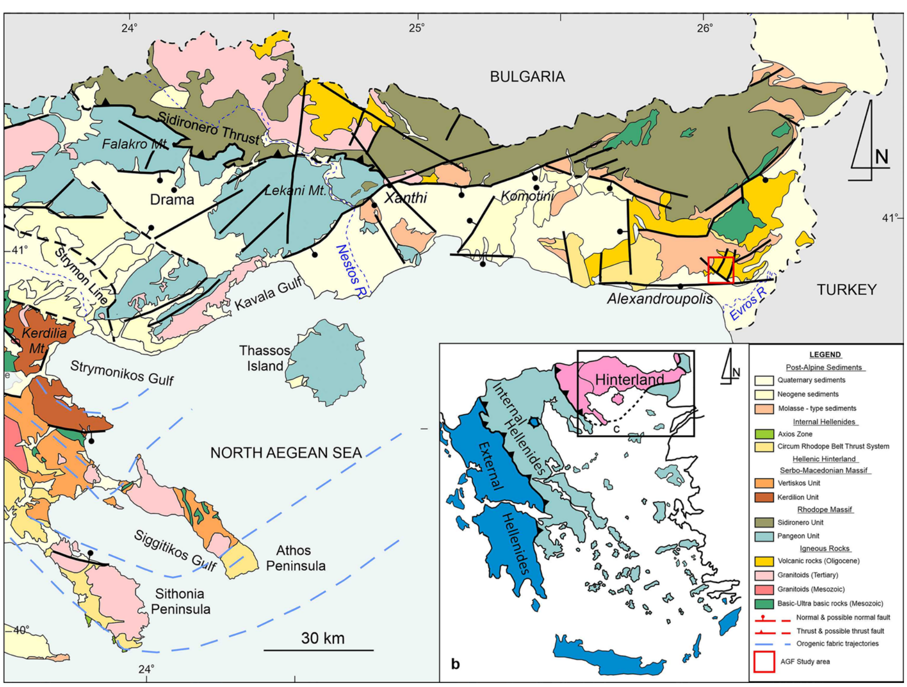

Fig. 1 Generalized geological map of northeastern Greece, indicating the main faults (modified from Tranos, 2009; Plougarlis and Tranos 2015) and the Aristino Geothermal Field (red frame)

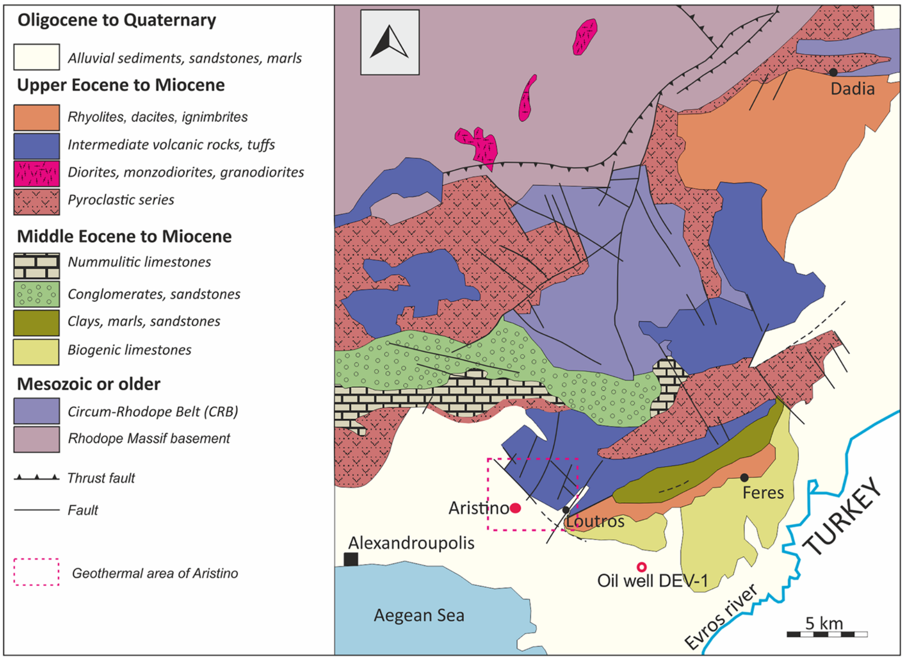

Fig. 2 Simplified geological map of the southern edge of the Evros river Tertiary molassic basin (from Christofides et al. 2004)

marginal fault, striking WNW–ESE (Fault 1, Fig. 3). These complexes are hereinafter referred to as follows:

- Unit A:volcanic province
- Unit B1:the southern submerged and thermally bounding area, with strong lateral groundwater infiltration to the depth of 150 m
- Unit B2:the transitional volcano-sedimentary area without any obvious groundwater inflow.

In the volcanic province (Unit A), the shallower aquifer of the upper system is developed at depths 100–200 m, whereas the top of the deeper aquifer is encountered between 110 and 250 m.

In the area where volcano-sedimentary sequences dominate (Unit B2), the shallower aquifer is encountered in low permeability formations, at depths of 190–210 m, overlapping an intermediate reservoir (in depths between 210 and 330 m). The deeper and most significant geothermal aquifer is developed at depths ranging between 330 and 430 m, inside high permeable ignimbrite.

The confirmed geothermal field covers almost 16 km^2, whereas the prospective thermally affected region probably exceeds 50 km^2. The water temperature within the first 500 m below ground surface ranges from 30 to 99 °C. The mean geothermal gradient varies from 40 °C/km in the southern part of the field (volcano-sedimentary area), to over 450 °C/km in the northern, volcanic province.

Two main chemical types of thermal water were identified (Poutoukis and Dotsika 1998; Kolios 2001; Kolios et al. 2005; Dalampakis et al. 2021): Na–Cl (SO_4) for the

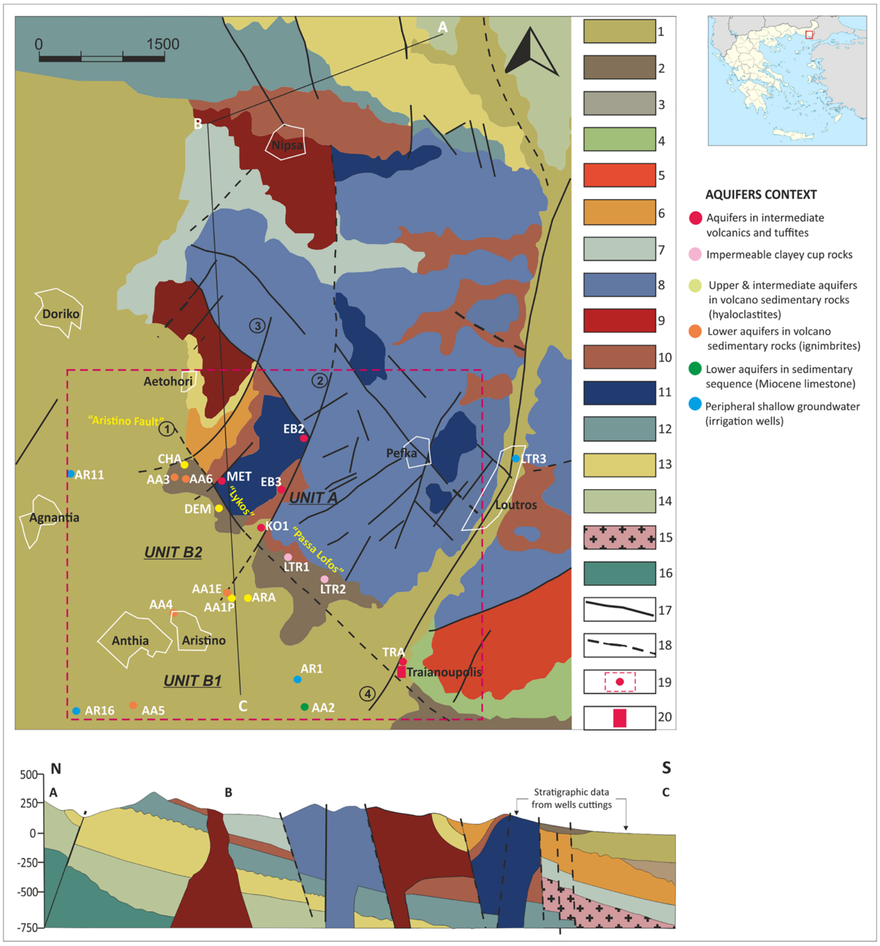

LEGEND: 1. Torrential deposits (Holocene), 2. Terrace systems (red clays to sandy clays) (Pleistocene), 3. Gray clays and conglomerates of volcanites and tuffs (Upper Pliocene-Pleistocene), 4. Oolotic limestones (Upper Miocene), 5. Rhyolites (Oligocene-Lower Miocene), 6. Clays, marls, and fine-grained sandstones (Oligocene), 7. Sandy-calcareous facies (Upper Eocene-Priabonian), 8. Dacitoid andesites (domes, dykes, pillow lavas) silicified and kaolinitized (Upper Eocene) 9. Rhyodacites (domes, dykes, pillow lavas)(Upper Eocene), 10. Tuffs-tuffites (Upper Eocene), 11. Andesites (domes, dykes, pipes), (Middle Eocene-Oligocene), 12. Nummulitic limestones (Middle Eocene-Upper Lutecian), 13. Clayey - marly series (Middle Eocene-Lower Lutecian), 14. Basic clastic series (Middle Eocene-Lower Lutecian), 15. Hyaloclastic volcanic breccia (ignimbritic flows), 16. Dolerites, spilites, 17. Fault, 18. Probable fault, 19. Prospected geothermal area, wells location, 20. Thermal spring discharge area.

Fig. 3 Geological map and cross section of the wider area of the AGF, simplified and compiled from Papadopoulos (1980). The southern part of the geological cross-section ABC, for depths up to 500 m, is based on wells cuttings examination. 1. Torrential deposits (Holocene), 2. Terrace systems (red clays to sandy clays) (Pleistocene), 3. Gray clays and conglomerates of volcanites and tuffs (Upper Pliocene–Pleistocene), 4. Oolitic limestones (Upper Miocene), 5. Rhyolites (Oligocene–Lower Miocene), 6. Clays, marls, and fine-grained sandstones (Oligocene), 7. Sandy-calcareous facies (Upper Eocene–Priabonian), 8. Dacitoid andesites (domes, dykes, pillow lavas) silicified and kaolinitized (Upper Eocene) 9. Rhyodacites (domes, dykes, pillow lavas) (Upper Eocene), 10. Tuffs-tuffites (Upper Eocene), 11. Andesites (domes, dykes, pipes), (Middle Eocene-Oligocene), 12. Nummulitic limestones (Middle Eocene–Upper Lutetian), 13. Clayey-marly series (Middle Eocene–Lower Lutetian), 14. Basic clastic series (Middle Eocene–Lower Lutetian), 15. Hyaloclastite volcanic breccia (ignimbrite flows), 16. Dolerites, spilites, 17. Fault, 18. Probable fault, 19. Prospected geothermal area, wells location, 20. Thermal spring discharge area

shallower aquifers of lower temperature (50–53 °C), and Na–Cl for the deeper, widespread, and hottest aquifers (up to 99 °C). Stable isotope contents (^{18}O and ^{2}H) indicate 2 processes: (a) the participation of marine solutions, based on mixing between a low chloride solution with one solution of high salinity, and (b) geothermal water exchange with hosting rocks (Poutoukis and Dotsika 1998). The chemical and isotopic geothermometers applied by Poutoukis and Dotsika (1998) and Dotsika et al. (2021) suggested deep equilibration temperatures in the range of 130–200 °C, further discussed in the closing chapter. The temperature of 146 °C was measured, after correction, in the basement of the Evros River Delta Basin, at the depth of 4200 m, inside the exploratory oil borehole DEV-1 (Fig. 2), 10 km SE of the AGF (Fytikas and Kolios 1979; Chiotis 1986).

The general objective of the present study is to bring together, synthesize, process, and reevaluate all relevant available data, as well as to present new information regarding temperature logs, thermal gradients, and heat flow assessment, emphasizing on the evaluation of the spatial distribution of temperatures. Furthermore, the authors make an attempt to (a) elucidate the complex structure and geometry of the AGF by determining the preferential fluids' upwelling paths/zones, (b) propose an initial thermal model, integrating all available thermometric data, and (c) identify the most promising production zones. Last but not least, the utmost goal and challenge of this paper is to contribute to the assessment of the presence (or not) of exploitable, deeper, medium enthalpy aquifers (*lower* hydrothermal system), that could be used for power production.

Geological setting

The study area (Fig. 2) is located on the southwestern margin (basement edge) of the Evros Tertiary Basin, which, in turn, constitutes part of the wider Thrace Basin, 14 km eastwards of the town of Alexandroupolis. The Thrace Basin is one of the largest Tertiary basins in the North Aegean region (Kilias et al. 2015), extending between SE Bulgaria, NE Greece, and NW Turkey. It has evolved on the high-grade metamorphic rocks of the Rhodope Massif, which occupies large parts of NE Greece and southern Bulgaria, as well as on the Circum-Rhodope Belt (CRB) and its easternmost counterparts. The CRB, with its low-grade metamorphic rocks, along with the Rhodope massif, constitutes the inner part of the Hellenic orogen, as the latter was formed during Alpine orogenic processes. The deposits of the Thrace Basin consist of thick molassic-type sedimentary rocks (3–5 km thickness) of Paleogene age, overlain unconformably by thick (1–2 km) Neogene-Quaternary sediments (Christodoulou 1958; Kopp 1965; Meinhold and BouDagher-Fadel 2010).

The peripheral low-mountainous terrains of the wider AGF area belong to the CRB, which in Thrace has been grouped into two tectonostratigraphic units (von Braun 1993): the mid-greenschist facies Makri Unit (conglomerates, sericite schists, calcschists and phyllites, limestones, and marbles, followed by volcanogenic and pyroclastic, metavolcanic rocks) (Papadopoulos et al. 1989; Magganas et al. 1991) and the tectonically overlying anchizonal Drimos-Melia Unit (dark gray shales, sandstones, and minor conglomerate beds, representing a sedimentary succession of a flysch-like character (Dimadis and Nikolov 1997).

The basinal part of the study area belongs to the Loutros-Ferres sub-basin (Fig. 2) of the broader Evros Tertiary Basin, which is the oldest sedimentary basin in the southern Hellenic Rhodope Massif (Caracciolo et al. 2015), and the widest and most affected by subsidence eastwards (Innocenti et al. 1984; Christofides et al. 2004). Thick Tertiary sedimentary formations unconformably overly the Cretaceous metasedimentary rocks of the CRB (Attri et al. 2012). The sub-basin is characterized by a basal clastic deposit (conglomerates and coarse-grained sandstones (Innocenti et al. 1984), overlain by clays and marls and, locally, Upper Lutetian nummulitic limestones. During the Priambonian transgression, molassic sediments, volcanic, and volcano-sedimentary rocks were unconformably deposited, whereas individual Oligocene basins were developed transgressively on the Priambonian formations (Michael et al. 1989).

The Tertiary sedimentation evolved in parallel with an intense syn-sedimentary magmatic activity with plutonic, subvolcanic, volcanic, and pyroclastic rocks. The volcanic products intercalated in the Priambonian series, and especially in the Oligocene marly-clayey sediments, are well developed and consist mostly of subaqueous and subaerial pyroclastic deposits.

Numerous ignimbrite units, recognized within the Oligocene series, can reach a thickness of some hundred meters (south of Dadia) (Innocenti et al. 1984). In the AGF area, the volume of pyroclastic products diminishes, whereas lava flows and domes become more common. The closure of the volcanic activity occurs in the early Miocene, with the emplacement of rhyolites to the southeastern part of the investigated area (Christofides et al. 2004) and the Agnantia ignimbrite to the west (Marantos 2004). The period of intense volcanic activity was followed by the deposition of Oligocene marine, brackish, and terrestrial sandstones, mudstones, marls, and conglomerates (Papadopoulos 1980), which reach their maximum thickness at the eastern part of the basin and wedge out westwards, as evidenced by the wells drilled down to the depth of about 500 m.

Pleistocene is dominated by torrential, river-mouth, eluvial-mantle, and marine terrace deposits. Quaternary sediments are mostly encountered south and southwestwards of Aristino. The low land area constitutes a collector basin, filled with coastal and river mouth deposits, pebbles, and coarse-grained sands.

All volcanic, volcano-sedimentary, and sedimentary formations cropping out in the wider AGF are shown in the simplified geological map in Fig. 3. The western sector of the AGF, where the major geothermal interest (Loutros-Pefka-Aetohori area) occurs, is dominated by magmatic rocks that intrude the Eocene clastic and marly-clayey sequences. Coarse tuffs, breccias, and lavas were emplaced mainly in a continental environment, with limited shallow marine influence (hyaloclastites and pillow lavas outcrops).

Lithological correlations from representative drillholes, as identified from cuttings examination, are shown in Fig. 4.

Most volcanic products (lavas domes and volcaniclastic) have been affected by intense hydrothermal activity, which is characterized by mineral zoning (silicic, argillic, sericitic, and propylitic zones), and, in places, by sulfate polymetallic mineralization (Michael et al. 1989; Arikas and Voudouris 1998; Marantos et al. 2007). Clay minerals constitute the main alteration products of volcanic rocks. They frequently replace volcanic glass almost entirely with smectites, forming outcrops of kaolinites.

As evidenced by the extended hydrothermal alteration to depths as great as 200 m in the Oligocene volcanics of Loutros-Pefka-Aetohori region (recognized in drillholes), the temperatures during Oligocene must have been elevated (Marantos et al. 2007). The latter is in accordance with the assumption of the volcanic activity culmination during the same period. The Oligocene–Miocene magmas were emplaced at shallow depths, along deep-seated detachment faults, forming plutonic, subvolcanic, and volcanic rocks

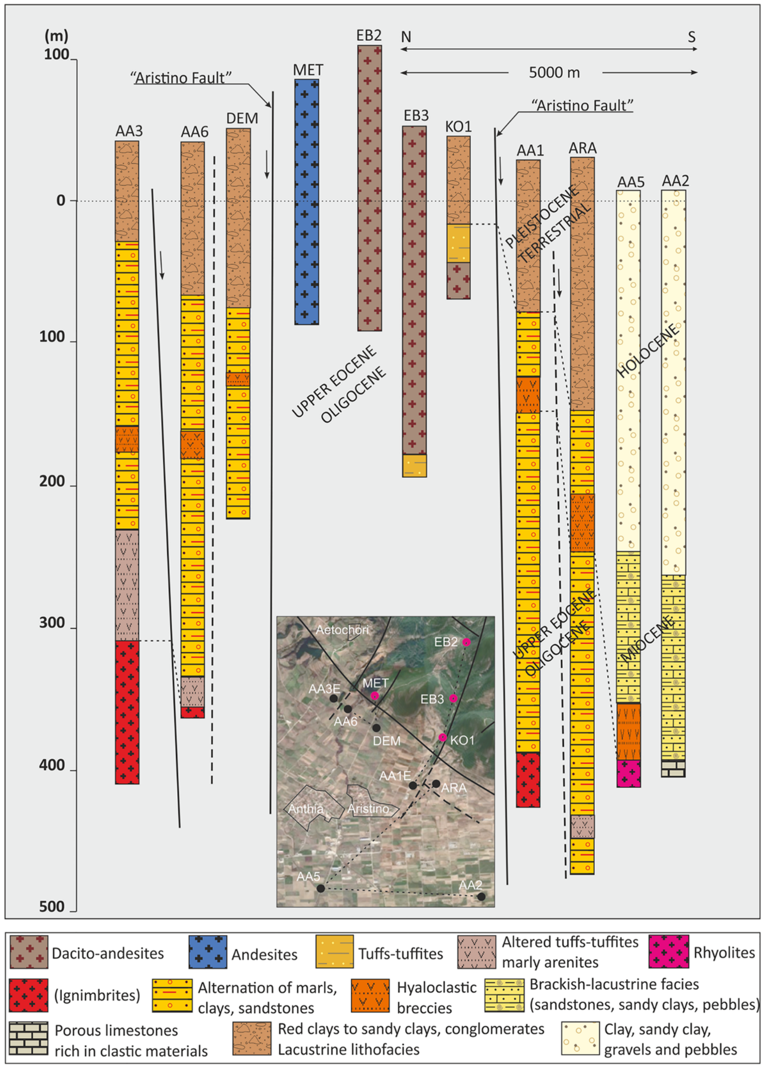

Fig. 4 Lithological correlations from representative wells

of calc-alkaline, high-K calc-alkaline, and shoshonitic affinities (Christofides et al. 2004; Marchev et al. 2005).

Tectonics of the Aristino-Traianoupolis geothermal area

Tectonic activity is responsible for the geomorphology of the wider AGF area and the presence of confined to semi-confined fractured zones, acting as pathways for vertical upwelling of thermal waters. The most relevant and thermally triggering tectonic structures are the intersecting NW–SE and NNE–SSW striking, oblique to dip-slip, normal faults.

Fault 1 (Fig. 3) is considered to play a crucial role in the development and geometry of the AGF, since it separates the volcanic province from the volcano-sedimentary sequences. This fault is hereinafter named as “*Aristino fault.*” Aristino fault, as well as Faults 2, 3, and 4 (Fig. 3), were activated by an N–S extension. In the areas intruded by volcanic rocks, both dominating strikes are associated with outcropping mineralized zones (amorphous silica and silica breccias) (Michael et al. 1989). The continuation and buried segments of the main active faults transecting the sedimentary sequences toward the south were detected after the interpretation of respective images from deep Electrical Resistivity Tomographies (ERTs), which were recently conducted by the Department of Geophysics of the Aristotle University of Thessaloniki (P. Tsourlos and G. Vargemezis, unpublished research, personal communication).

The subparallel NNW–SSE faults were identified in both volcanic and volcano-sedimentary provinces, with the "Aristino fault" constituting the dominating regional tectonic structure. A shift in Aristino fault's strike can be traced toward the east, where strikes from NW–SE to almost WNW–ESE. In its eastward's extension, Aristino fault bounds Loutros-Ferres sub-basin and separates the northern uplifted volcanic province (andesites, dacito-andesites and rhyodacites in the form of domes, dykes, submarine extrusions, and pillow lavas) from the southern stepwise subsided province, filled with sedimentary and volcaniclastic Paleogene to Holocene formations. This subsidence of the eastern part of the study area toward the south, as well as the geomorphological separation of the low-mountainous terrain from the basinal plane, is caused by the most recent activity of generally E–W striking fault segments as normal faults.

All the NNE–SSW striking faults (2, 3, and 4—Fig. 3) affect mainly, from north to south, the volcanic edifices, as well as the Paleogene volcano-sedimentary sequence that is covered by the Pleistocene deposits of the lower terrace system. These faults, with minimum lengths between 3.5 and 8.5 km, were initially active from Oligocene to Miocene, as strike-slip faults (Tranos 1998, 2009, 2011). They have, however, been reactivated in more recent times, affecting the Neogene and Quaternary sediments (Rondoyanni et al. 2004). Their overall kinematics is complicated.

Fault 2 has a visible length of 8.5 km, with the associated fractured zone transitioning to "damage zone" at the proximity of its intersection with the "Aristino Fault." Fault 2 runs between the volcanic domes of "Pasa Lofos" and "Lykos" (Fig. 3), affecting the Tertiary volcanic and sedimentary rocks to the north. This active structure exhibits a well-preserved vertical slickenside, 30 m to the east of the well KO1, which was drilled on the hanging wall of Fault 2 (Fig. 5). Its buried segment continues for at least 700 m toward the south, as evidenced by the application of Transient Electromagnetic Method (TEM) prospecting (Karmis et al. 2004). The latter is also supported by the temperature flexure in the vicinity of the well AA1E (drilled along the fault line-Fig. 3), in comparison to the temperature regime of the wells AA4 and ARA, located westwards and eastwards of the fault, respectively (Fig. 6a).

The 3.5–4 km long "Fault 3," is the dominant tectonic structure at the northwestern side of the AGF. It can be traced in the area north of the production wells CHA, AA3, and AA6, affecting the Pleistocene and Neogene sediments and the altered volcanic and volcano-sedimentary rocks (Fig. 3). Its buried segment continues for at least 1000 m to the southwest, as depicted in Fig. 7 after the interpretation of the Electrical Resistivity Tomographies (ERTs) sections AB and CD, which are part of 2 long profiles (2400 m) deployed in this part of the AGF. Both sections confirm the presence of the Aristino fault and Fault 3, regarding both visible and buried segments. The results are based on the interpretation of images from inversed 2D deep ERT. The maximum prospecting depth is 500 m. Numbers 1–8.2 in Fig. 7 represent different lithological units and

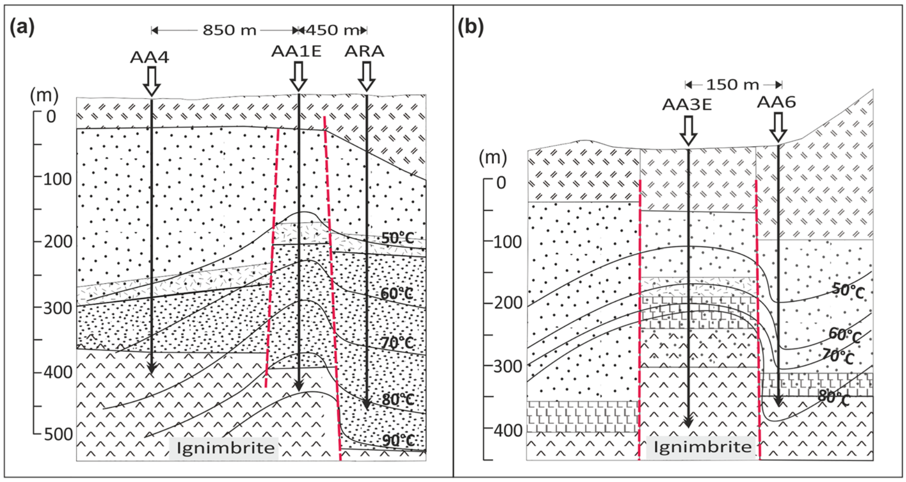

Fig. 5 (**a**) Fractured zone across the buried segment of "fault 2" to the south and (**b**) Buried segments of the intersected Faults "3 and 3.1." Both show isotherms flexure due to the upwelling of thermal waters in the form of well-oriented "heat intrusions" through fault-controlled damage zones

Fig. 6 Fault-plane with vertical slickenside of the normal fault 2 exposed at the west side of the Pasa Lofos rhyo-dacitic dome

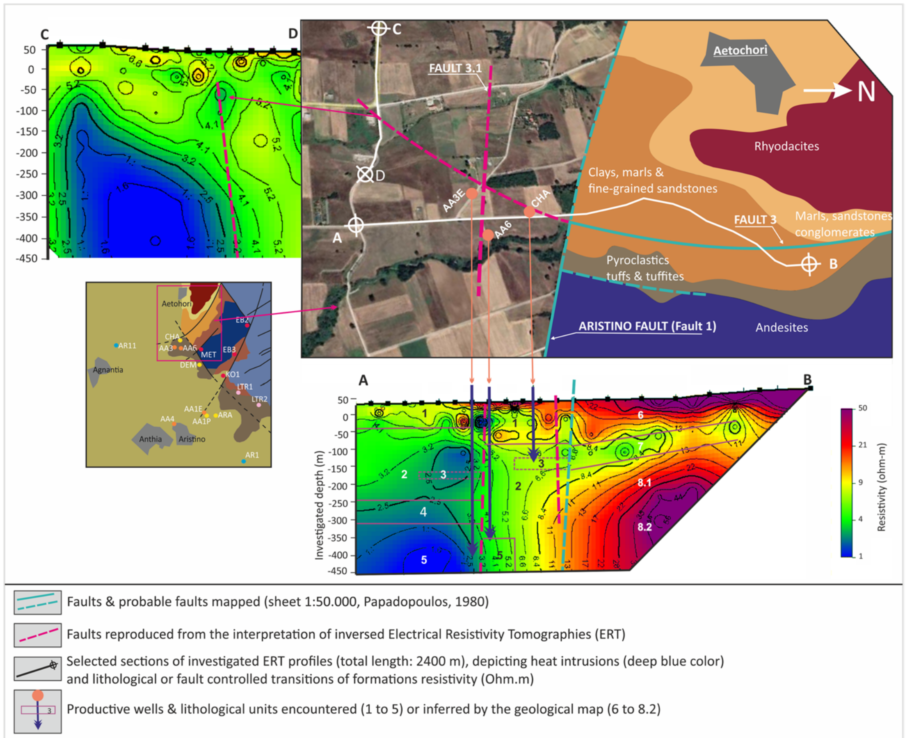

Fig. 7 Identification of the "Aristino fault" and Fault 2 buried segments and a new buried fault transecting the area between AA3 and AA6 productive wells in agreement with Fig. 6b. (Tsourlos and Vargemezis––unpublished research)

transitions, either encountered during the drilling of the three above-mentioned boreholes or inferred by the geological map. Unit 5 corresponds to the lower aquifer inside the ignimbrite.

A new buried fault, parallel to "Aristino" fault, is also identified between the wells AA3 and AA6 (Fig. 7). Its intersection with Fault 3 is likely to be very critical for the upwelling of hot water in the form of directed heat intrusions, as indicated from the bell-shaped deep blue-colored areas, representing extremely low resistivity values (1–2.5 Ohm.m). The latter is also evidenced by the 70–80 m throw of the volcanoclastic breccia (ignimbrite), revealed by the examination of cuttings in the adjoining wells AA3 (footwall) and AA6 (hanging wall), as well as by the sharp inflection of the isotherms through the fractured zone from the down-dropped to the raised block (Fig. 6b). Such deep intersecting faults may be responsible for the establishment of large enough "damage zones," which enhance secondary permeability, thus facilitating the vertical movement of the geothermal fluids.

This group of NNE–SSW striking faults ends eastwards with the seismically active "fault 4" that has shaped the course of "Tsai Rema" (Fig. 3). With a visible length of 11 km, it composes the western edge of the Evros River lowering (Rondoyanni et al. 2004). This fault transects the volcanic rocks and the Eocene, Neogene, and Quaternary sediments, assuming successive phases of reactivation in various geological periods until today. The latter may apply to all other respective tectonic structures with similar kinematics to the west.

Comprehensive temperature survey of Aristino-Traianoupolis geothermal area

The temperature survey of Aristino-Traianoupolis geothermal area was based on data acquired by periodical, non-continuous, in situ measurements in geothermal or irrigation wells. Continuous temperature loggings were exclusively performed in uncased wells a bit before the production casing was set. These measurements, which are strongly affected by the drilling mud circulation, are not reliable indicators for the assessment of formation's temperature and they have not been taken into account in the present study. The compilation and analysis of subsurface temperatures constitutes a very useful tool to illustrate spatial and vertical distribution of temperature, characterize the heat mode transfer, and to evaluate the effects caused by active tectonics and heat flow anomalies.

Field measurements

Subsurface temperatures were obtained by temperature–depth measurements in sixteen (16) decommissioned and three (3) producing wells (Table 1 and Fig. 3).

These wells have never been put into operation, which means that the thermal state of the field has remained undisturbed, and all acquired data can be considered as representative of the formation's temperature. Moreover, it must be mentioned that the geothermal system does not undergo transitional flow, since no notable surface discharging points exist, except for one thermal spring at the eastern part of the field (Fig. 3), with very low artesian flow rate (–7 m^3/h).

Downhole temperature measurements were conducted at various time periods, long after the completion and/or pumping of the wells, at regular depth intervals of 10 m, by using reel portable thermometers with a platinum (Pt100) temperature sensor connected to an electrical conductor logging cable. Except for two abandoned slim boreholes (LTR1 and LTR2), located in the clayey impermeable cap, all the rest are water filled from, fully or partially penetrated, hot aquifers. Some of the most critical wells (KO1, EB3, AA4, and AA5) are either totally damaged or have serious casing failures and, consequently, are no more accessible for repetitive measurements and further evaluation. The rest of the wells are accessible to the bottom end. The observation and analysis of the obtained temperature–depth profiles were particularly useful for the identification of spatial and vertical distribution of subsurface temperatures and depth variation, the calculation of temperature gradient, and the assessment of heat flow distribution.

Spatial distribution of subsurface temperatures and depth implications

Based on the measured downhole temperatures, representative temperature–depth contour maps were constructed, providing a good estimation of how temperature is distributed at specific depths, and how depth changes for a specific temperature.

The isotherms illustrated in Fig. 8 were plotted from data that exhibit considerable scatter in some areas, due to the absence of observation wells or to the temperature differences between neighboring deep and shallow wells. Nonetheless, the contour maps in Figs. 8, 9 can provide critical information for the subsurface temperature distribution in the investigated geothermal area.

The isotherms in Fig. 8 represent the distribution of temperatures at shallow depths. The maps illustrate the main upwelling areas, which are associated to the most relevant

Table 1 Data related to temperature profiles obtained from unused wells

Symbol/Type/Year of drilling	Altitude amsl (m)	Depth max (m)	Thermal gradient (°C/1000 m)	Interval (m)	Maximum temperature (°C)
KO1/P/1988	56	116	500/175	20–100/100–120	80 (PT)
LTR1/SH/1994	58	113	140	20–100	34 (BH)
LTR2/SH/1994	56	153	110	30–140	33 (BH)
EB2/P/1994	119	210	184	20–190	52.5 (BH)
EB3/P/1994	65	253	230/433/100/330/200	20–120/120–150/160–170/180–250	92.5 (BH)
TRA/P/1984	15	52	Artesian Flow		51
MET/P/2007	83	170	240	20–110	44
AA1/SH/1999	30	465	170/60/140	20–190/190–200/200–400	89.5 (BH)
AA2/SH/1999	10	410	40	20–350	30.5 (BH)
AA3/SH/2000	44.10	450			
AA3/P/2000	43.46	360	200/100/460/Isothermal	20–200/200–220/220–280/280–360	89.2 (PT)
AA4/P/2000	24.3	430	96/138/110/Isothermal	20–240/250–280/290–380/390–430	64 (BH)
AA5/P/2000	7.23	420	40	20–420	32.8 (BH)
AA6/P/2016	43.23	410	45/112/162/342/152/240	30–60/70–120/130–170/180–190/200–360/370–400	75–77 (BH) 99 (PT)
ARA/P/2004	29.45	500	160/60/120	20–250/250–270/280–480	80.3 (BH)
CHA/P	45.35	200	238/115	20–160/170–180	57 (BH)
DEM/P/2003	49.6	300	242/184	20–150/160–260	73.3 (BH)
AR11/P	40	140	90	20–140	26.5 (WH)
LTR3/P	28	150	Isothermal/80	0–130/140–150	25.9 (BH)

KO1	Extremely high thermal gradient 45 °C/100 m in the first 100 m of highly altered and impermeable caprocks with clayey, tuffaceous materials, and altered dacite with sulfides mineralization. Fractured dacites between 110 and 120 m. Flow rate: 20 m^3/h
LTR1	Rectilinear temperature profile and high gradient. Slim decommissioned well in the red clayey part of the cap rock
LTR2	Well, decommissioned in the red clayey part of the cap rock. High gradient in the first 100 m. Lateral thermal outflow

Table 1 (continued)

EB2	Altered dacites. No significant water flow rate (< 10 m^3/h). High mean gradient. Gradual deepening of isotherms northwards
EB3	Gradient remarkably high for almost overall profile apart from a limited convex upward inflexion between 150 and 170 m. Highest static temperature 92.5 °C at 250 m depth. Lower aquifer in low permeability tuffites in the last 10–20 m. Flow rate 40 m^3/h
TRA	Thermal spring discharge area. Well in high fragmented rhyolite with artesian flow. Pumping rate > 120 m^3/h when tested
MET	Rectilinear conductive profile. High thermal gradient. Aquifer in low permeability volcanic rocks, at 160–170 m
AA1	Nearly rectilinear temperature profile. Between 190 and 200 m. upper aquifer in volcaniclastics. High mean thermal gradient
AA2	Overall profile rectilinear. Minimum background thermal gradient (42.5 °C/1000 m) for the entire exclusive area
AA3	Casing until 354 m. Inadequate critical information for the vertical extension of the convective system in the ignimbrites

Table 1 (continued)

AA3	Irregular temperature profile. Conductive 20–200 m and 220–280 m. Rectilinear temperature increment with sharp break in the lower segment presumably due to the extremely low thermal conductivity of the clayey formation. Upward convective cell 200–220 m (upper aquifer). Isothermal profile 280–360 m. Maximum temperature 89.4 °C. Flow rate > 100 m^3/h
AA4	Temperature profile nearly rectilinear with minor irregularities. Trend for isothermal evolution in the basal part
AA5	Temperature profile identical with those of the well AA2
AA6	Drilled on the hanging wall of the active Fault 3. Hottest temperature measured in the AGF (99 °C) with a continuous upward trend after a 75 h pumping test, due to lateral advection triggered by the continuous water level drawdown. The BH temperature has undergone a gradual but strong cooling down process before equilibration at 78 °C after 24 months
ARA	Adjacent to the well AA1E. The deepest well in the field. Lower aquifer (ignimbrites) not reached. Max flow rate 25 m^3/h at 65 °C from low permeability intermediate aquifers in volcano-sedimentary sequences. High mean thermal gradient
CHA	High thermal gradient for overall profile. Tapping in the Upper volcano-sedimentary aquifer with maximum flow rate 25 m^3/h

Table 1 (continued)

DEM	Rectilinear thermal profile. Gradient remarkably high. Main productive formation not reached. Max flow rate 25 m^3/h
AR11	Irrigation well 1220 m westwards of the AA3 well, in a fractured zone, bounding the western edge of the geothermal area
LTR3	Irrigation well with artesian flow, 2600 m north of the Traianoupolis thermal spring within low cohesion sediments

P Production, *SH* Slim hole exploratory well, *PT* Measurement at the end of pumping test, *BH* Bottomhole measurement, *WH* Measurement at the well head

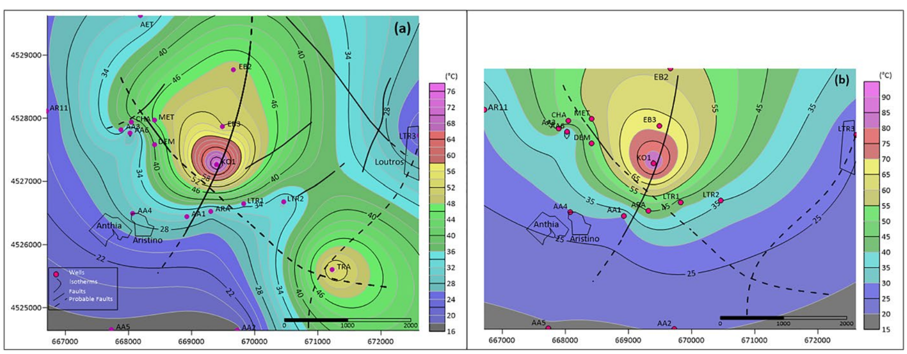

Fig. 8 Plot of isotherms: **a** at 50 m depth bmsl (close to the ground surface for the largest part of the AGF) and **b** at 100 m bmsl (absolute depth between 110 and 220 m)

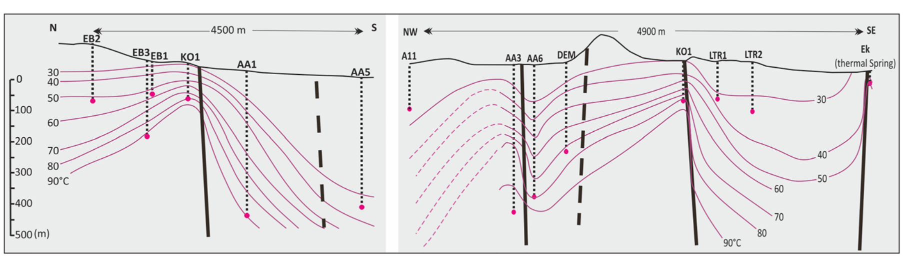

Fig. 9 Sections N-S & NW-SE with vertical and lateral distribution of temperatures

upward leakage zones in the vicinity of intersected blocks related to the "Aristino fault" and faults striking NNE–SSW. These zones are also characterized by heat accumulation, along with the highest temperature and thermal gradient values for similar depths. The isotherms for depths greater than 100 m bmsl can be considered reliable solely for the main geothermal anomaly area where most of the wells were drilled at adequate depths. There are no available data for the southeastern part of the AGF for depths greater than

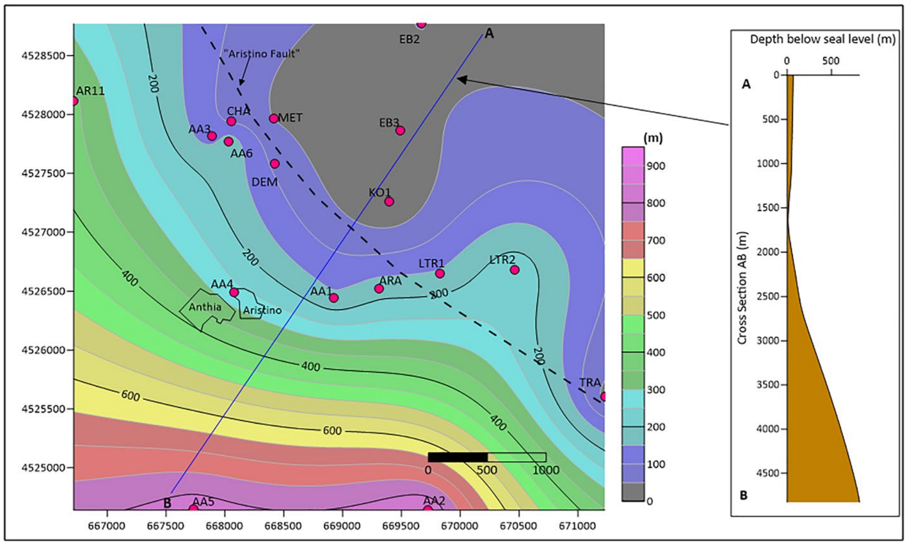

Fig. 10 Iso-depth contour map for $T = 50$ °C. Data for the wells AA11, LTR1, LTR2, AA2, and AA5 have been retrieved from the extrapolation of their conductive thermal profiles at secure depths to 500 m

50–60 m, which is the maximum depth of the (artesian) wells drilled in the Traianoupolis thermal spa center.

The vertical and lateral distribution of temperature is largely affected by the presence of a few meters wide fractured zones, enabling the upward movement of deeply heated geothermal fluids. As clearly shown in the cross sections in Fig. 10, where temperatures at depths up to 460 m have been incorporated, such vertical movement distorts the temperature isolines in the upper conductive segments, forming well-localized "bell-shaped" thermal plumes, followed by a broad lateral heat transfer away from the faults, unevenly to all directions.

All major thermal anomalies occur either in areas not covered by adequate cap formations (volcanics) or in the vicinity of the main leakage fractured zones. The distribution of temperatures, as retrieved from boreholes' data, indicates an area of hydrothermal anomaly that covers at least 13 km^2.

Figure 9 shows the iso-depth contours plotted for a constant temperature of 50 °C. The AB cross section shows a sharp deepening of the isolines southwards of the "Aristino fault." The transition from the volcanic province to the sedimentary basin is characterized by a (sub)parallel to this fault development of the iso-depth contours.

The dipping rate (in meters per km of distance) for similar temperatures could constitute a useful tool for an initial assessment of anticipated target depths. An estimation of the dipping rate changes has been applied to the volcano-sedimentary Units B2 (hotter) and B1 (cooler) (Fig. 11), considering the wells DEM and AA5 as starting and end points, respectively. This approach shows that for temperatures 30–80 °C, the targeted depths change unevenly with the dipping rate between the 2 Units, being almost 2 times higher in Unit B1 (AA4–AA5), than the respective one in Unit B2 (DEM–AA4).

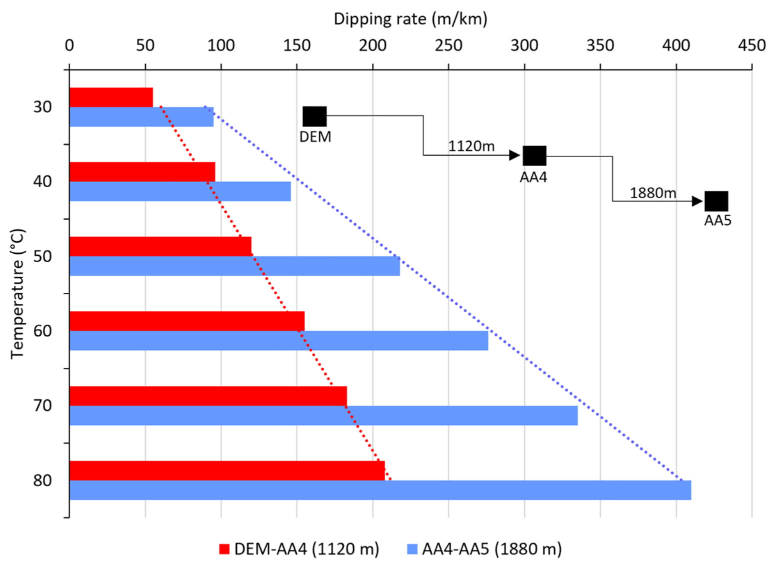

Fig. 11 Plot of the dipping rate (m/Km) of depth for temperatures ranging from 30 °C to 80 °C

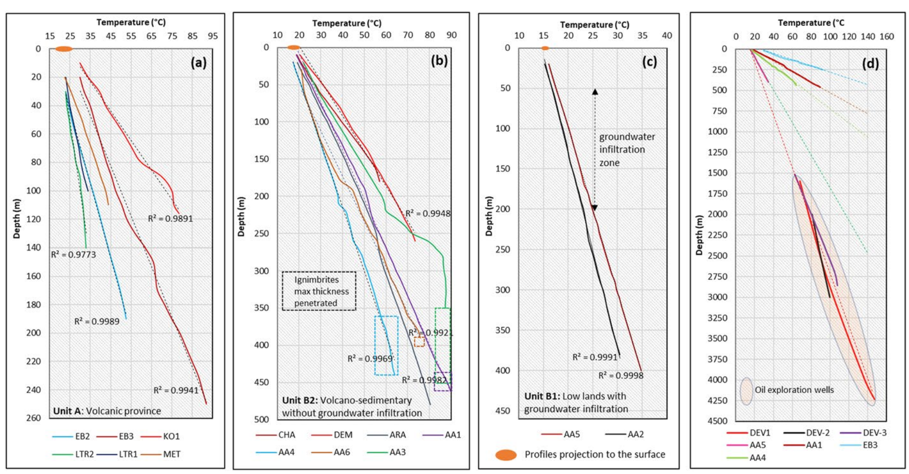

Fig. 12 Depth vs temperature plots of the wells investigated in the AGF area in various structural and lithological environments

Vertical distribution of subsurface temperature

The temperature profiles shown in Fig. 12 are representative of the thermal regime in the 3 distinct lithological and hydrogeological units (A, B1, and B2) and constitute the basis for thermal gradient calculations.

In Units A and B2 the temperature increases significantly with depth, whereas in Unit B1 the rate of increase is much lower and consistent with the minimum geothermal gradient in this part of the study area. The linear regression equations show correlation coefficient (R^2) values > 0.98, with the majority being higher than 0.99, indicating an exceptionally good linear and positive correlation between depth and formation temperatures.

In Unit A, where the highest temperatures at very low depths were measured, there is no significant impermeable caprock formation. This is partially counterbalanced by an intense, deep-down widespread hydrothermal alteration (kaolinitization and silicification) (Michael et al. 1989; Marantos et al. 2007), which is responsible for the formation of a self-sealed semi-impervious formation developed at relatively low depths (100–200 m), favoring the more rapid heat transfer to the surface. Consequently, such a semi-protected system should undergo much greater thermal losses. This could explain the increased ground surface temperatures (17–24 °C), resulting from the extension of the rectilinear parts of the temperature/depth curves in all profiles (Fig. 12a). This is more evident for the well KO1, located within the damage zone of Fault 2.

In Units B1 and B2, the main deeper (330–500 m) aquifer of the upper system is overlain by thick clayey sediments of low permeability (cap rock), which obstruct the thermal transport and, thus, reduce the rate of thermal losses.

In Unit B2, the profiles of the AA3, AA6, DEM, and CHA wells (Fig. 12b) intersect the land surface at temperatures 0.8 to 2.8 °C higher than the mean annual value (15.2 °C). As regards the deep boreholes AA2 and AA5, which are representative of the thermal regime in the southern, cooler part of the AGF, the curves in both cases intersect the ground surface at about the mean annual temperature, which is also close to the temperature of the shallow aquifers in the area (16 °C, Well AR1) (Fig. 12c).

In general, the temperature profiles depict various features, such as abnormal gradients, rectilinear conductive evolution for almost all cases, downward curvature in the upper section of the well AA6, an isothermal section in the bottom segment of AA3, and nearly isothermal for isolated segments restricted to the shallowest hot aquifer in the area (AA1, ARA, AA3, AA4, and EB3) (Fig. 12).

The above features can be largely attributed to the lateral movement of water that transfers substantial amounts of heat at distant areas, away from the upwelling zones. The minor or major change of the profiles slope is related to stratigraphic changes and discontinuities, which are followed, in some cases, by a sharp increase of the thermal gradient, indicating very low thermal conductivities. As a result, stemming from the temperature distribution pattern in both Units A and B, the heat losses to the surface are mainly attributed to conduction, at least for the depth investigated so far (−500 m).

Figure 12d shows the profiles for the neighboring deep exploratory oil wells (DEV1, DEV2, and DEV3) based on corrected temperatures at only four depths. In the same plot, the extrapolation of some indicative conductive profiles in Units A and B is cautiously presented as a rough assessment of the expected depth for the maximum bottomhole temperature of 140 °C that was measured in DEV 1 and is in agreement with the lowest accepted values suggested by the applied geothermometers for the AGF area (Poutoukis and Dotsika 1998; Dotsika et al. 2021). The above, can be more securely considered for Unit B1, where the wells AA2 and AA5 are representative of the out-bounding and undisturbed local geothermal gradient. On the contrary, for Units A and B2, which are characterized by abnormal thermal gradients, such an approach may lead to non-credible and invalid results.

The profiles of Fig. 12 depict the main upwelling zones alongside the feeding zones and the lateral movement of hot water, with gradual drop of temperature when moving far from the discharging faults (Fig. 13). The temperature declines more abruptly

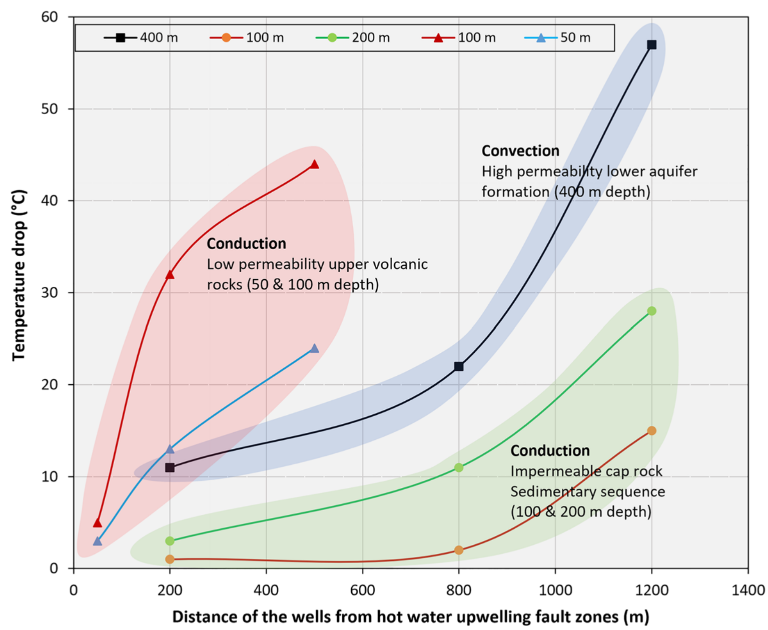

Fig. 13 Drop of temperature (°C) vs distance from the main fractured zones for various depths as depicted by the color of lines in legend

at distances greater than 800 m in Units B1 and B2 (volcano-sedimentary sequences), while in Unit A (volcanic province) thermal losses seep more steeply in the first 200 m away from the faults, being alleviated at a distance between 200 and 500 m. The latter, better matches with the highest rates of thermal losses along the most active fractured zones (highest calculated thermal gradients) and the widespread lateral thermal dissipation.

Conclusively, it can be assumed that in the vicinity of the main hot water-bearing fractured "damage" zones, geothermal fluids can potentially move upwards, discharging water and heat to the near-surface environment. In distant areas from the damage zones, lateral flow dominates, due to the widespread emplacement of the hosting permeable formations (volcanoclastic breccias and ignimbrites).

In Unit B1 the overall temperature profiles are indicative of a highly conductive regime within the upper 420 m. Both wells AA2 and AA5 (Fig. 12c) exhibit low bottomhole temperatures (32 and 35 °C, respectively) and the lowest mean thermal gradients (42–50 °C/km) in the AGF. Water samples from both wells show hydrochemical affinities (Kolios 2001; Kolios et al. 2005) with samples from Unit A and B2, indicating lateral water flow from north to south within the most permeable volcaniclastic formations. The sharp drop of temperature is related to the stepwise subsidence of the basin, the increase of the sediments' thickness, and the decrease of the heat flow. The thermal gradients in this Unit can be taken as reference values, although they remain anomalous compared to the gradients (30–32 °C/km) determined in the oil wells drilled in the deepest and neighboring parts of the Evros Delta basin.

Similarly, almost all profiles of Unit B2 have a quasi-linear trend, indicating a highly conductive regime from the ground surface to the maximum penetrated depth of 500 m (Fig. 12b). The only case deviating from this rule is the production well AA3, which exhibits an isothermal evolution at the lowest 70 m section. The bottommost 6 m of this section corresponds to a permeable ignimbrite layer, while the remaining 60–65 m could be correlated to an impermeable clayey formation of very low thermal conductivity. Such a lithology leads to the assumption that the isothermal pattern in this occasion is attributed to the presence of casing screens, which allows vertical convective flow between the well itself and the annular space between the casing and the formation.

Though only the topmost of the ignimbrite reservoir was reached by the production well AA3 (only the first 6 m), long-duration (5 days) pumping tests with a constant production rate of 100 m^3/h resulting to a total water level drawdown of 43 m, confirmed its high potential. Considering that this key formation was penetrated for at least 100 m in the nearby exploratory well AA3E (Kolios 2001) and assuming that the secondary permeability affects the entire formation, the anticipated performance of future wells drilled at similar depths (450–500 m) will probably be even better.

The above considerations favor the hypothesis for the presence of an extended vertical convection system within the ignimbrite reservoir. In this case, the lowest segment of the isothermal section is likely to be the uppermost part of a downward established convection cell, affecting a wider area of almost 6 km^2. In the AGF ignimbrites are met from north to south in the wells AA3, AA6, AA1, AA4, and AA5, the water samples of which exhibit common hydrochemical affinities (Kolios, 2001; Kolios et al. 2005). The expected transition to the convective regime cannot be adequately supported by the profiles since the ignimbrite formation has not been fully penetrated.

In the AA3 well, the volcano-sedimentary formation that overlays the ignimbrite acts as a thermal barrier. The sharpness of the transition in the successive temperature profiles between 220 and 280 m indicates the presence of an impermeable layer of very low thermal conductivity (aquiclude) that inconclusively––for the time being––corresponds to the bottom end of the conductive regime. Such abrupt thermal transitions are also observed in the temperature profiles of the wells KO1, EB3, and AA4 at various depths and thicknesses, illustrating stratigraphic variations and discontinuities.

In Unit A, all the temperature profiles up to the maximum investigated depth of 250 m show a clear conductive configuration, with minor deviations from almost perfect linearity (Fig. 12a).

Due to the scattered borehole points and the large divergence of the thermal gradient values, the high temperature increase rate with depth in Units A and B2 is likely to represent a localized anomaly resulting from circulating hot fluids at low depths that heat excessively the overlying rocks. According to Chapman and Rybach (1985) and Turan et al. (2016) such localized anomalies are common in low porosity hydrothermal systems with a near-surface leakage of hot water, mainly due to secondary permeability.

The maximum measured static bottomhole temperatures are 92.5 °C (EB3 at 250 m in Unit A) and 89.5 °C (AA1E at 460 m in Unit B2). All production wells showed that water temperature during the pumping tests is constantly higher than in static conditions (divergence from 2 °C to 24 °C). So far, the maximum known temperature in the

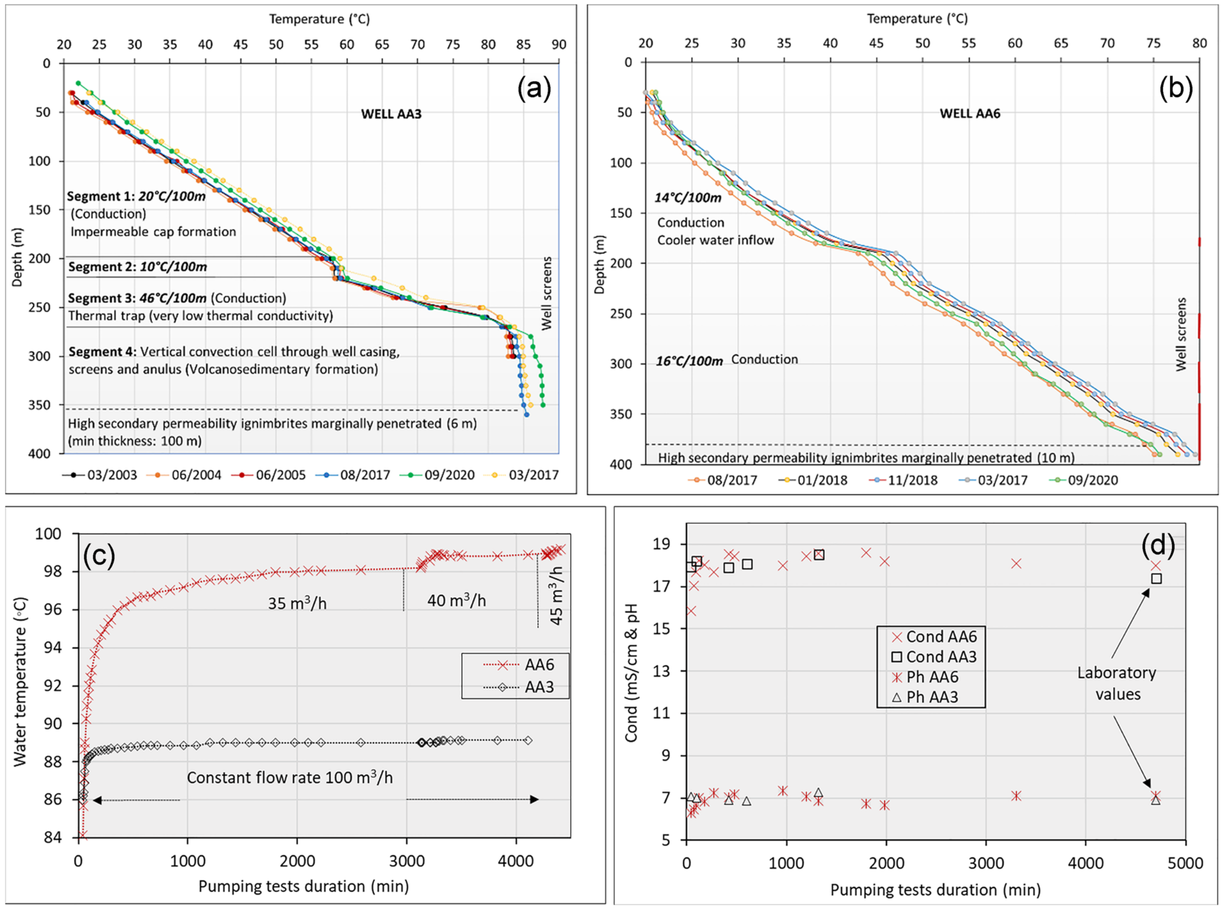

Fig. 14 Periodical temperature–depth logs (**a**, **b**) and records of water temperature (**c**), conductivity and pH (**d**) during long-duration pumping tests (down) in the wells AA3 and AA6

AGF is 99 °C, measured at the final stage of a 5-day-long pumping test performed on well AA6 (Fig. 14c).

This surprisingly high and constantly increasing temperature in AA6 well is 21–24 °C higher than the bottomhole static one (75–78 °C), measured long (12–18 months) after the end of the pumping test. The static temperature in AA6 is 8–10 °C lower than the corresponding one in the nearby production well AA3. This notable difference is even greater (27–28 °C) at the depth of 280 m, which represents the bottom end of the thermal trap in the well AA3, as clearly shown in the successive temperature–depth plots (Fig. 14a, b). The continuous, post-pumping, cooling down effect in AA6 was being recorded for 20 consecutive months before equilibrium was achieved at 78 °C, which is the maximum bottomhole static temperature in this borehole. Such an unexpected thermal response in AA6 was quite puzzling, since the two wells that are drilled at almost the same depth, very close to each other (150 m), are hydraulically connected and have the same hydrochemical characteristics.

However, the recently performed ERT has revealed the existence of a buried fault (Fault 3.1, Fig. 7), that transects and dislocates the area between the two wells (AA6 located at the hanging wall). This fault, in combination with the observed stratigraphic discontinuities, plays a critical role in the thermal behavior differentiation of the wells.

Water movement in AA6 is mainly driven by advection due to the high water level drawdown (> 60 m), which subsequently triggers the gradual inflow of hotter fluids from a laterally expanded, and presumably hydraulically connected, aquifer, with feeding zones in the adjacent volcanic province where temperatures much higher than 100 °C are expected at depths equivalent to those prospected (350–450 m) hereon.

Such high increase of the water temperature during pumping (up to 25 °C) has been recently described by Piscopo et al. (2020) for the hottest and more active hydrothermal systems in the island of Ischia (Italy), being attributed to the increased upwelling of deep hydrothermal fluids during pumping. However, this does not sufficiently explain the completely different thermal response of the two wells (AA3 and AA6), unless we assume a vertical thermal stratification in the suspected underlain convective system of the ignimbrite, triggered in both cases by different and well-contrasting top–bottom reservoir temperatures during pumping.

Thermal gradient assessment and evaluation

Thermal gradient calculations were conducted for all available wells. The distribution patterns of mean thermal gradients (Fig. 15) represent a staring local perturbation that is consistent with the geological, stratigraphic, and structural evolution of the geothermal area.

In the cooler lowland area, as indicated by the wells AA2 and AA5, the vertical distribution of thermal gradient, plotted in the blue-colored frame (Fig. 15a), does not show any significant deviation from the mean value of 42 °C/km. The majority of the other wells follow a general trend of gradual decrease with depth (orange-colored frame, Fig. 15a). The pink-colored area in Fig. 15a, includes the extremely abnormal gradient values (positive and negative peaks) observed in the wells AA3, AA6, KO1, and EV3, which are attributed to local lithological heterogeneities and, subsequently, to variations in thermal conductivity.

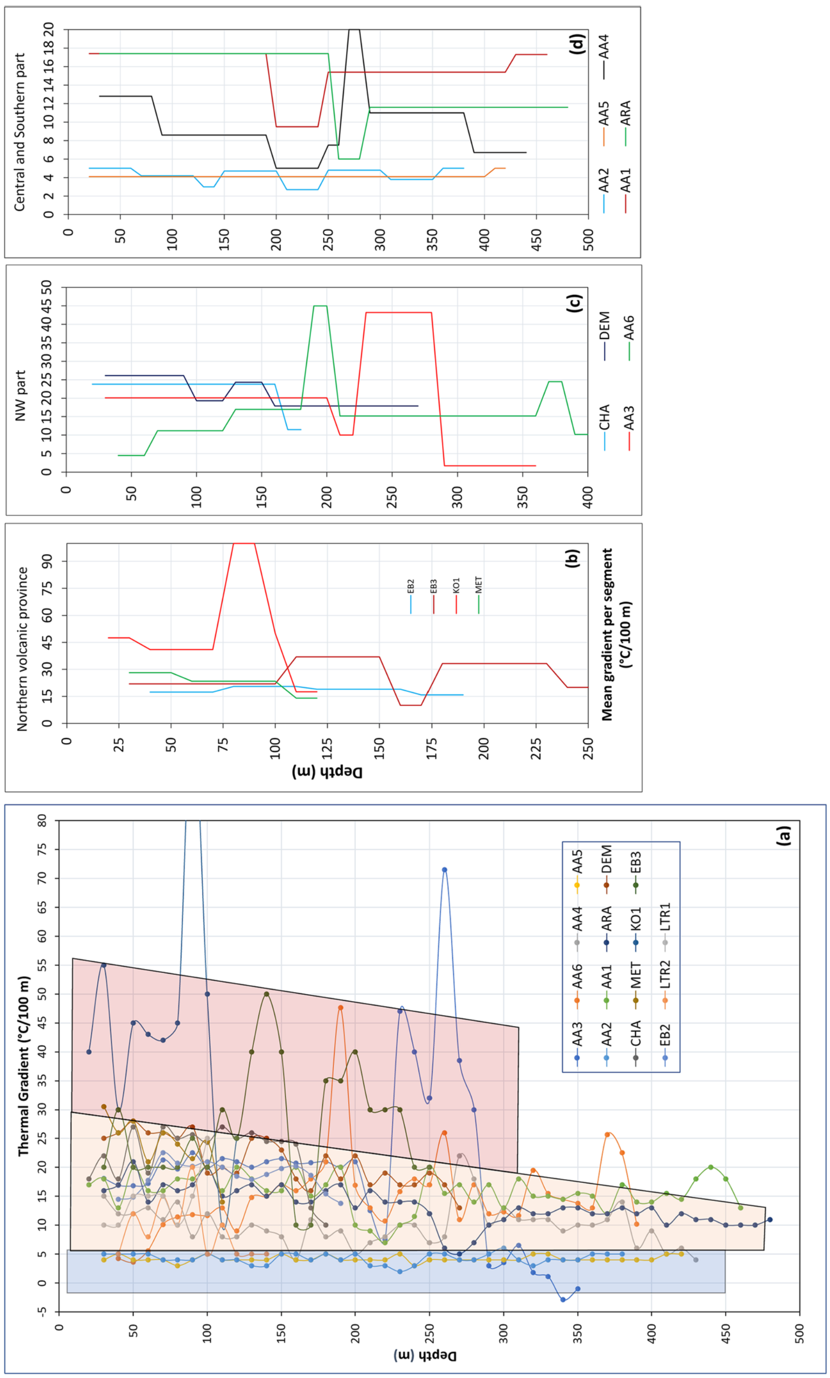

Fig. 15 Thermal gradient profiling in the AGF. **a** Vertical variation of thermal gradient profiles based on 10 m regular downhole temperature measurement steps. **b–d** Mean thermal gradient distribution per segment in various lithological units. Mean values are relative to the segments in the temperature profiles with common features: continuous temperature distribution, stratigraphic affinities, isothermal evolution, and significant changes in slope of the temperature profiles

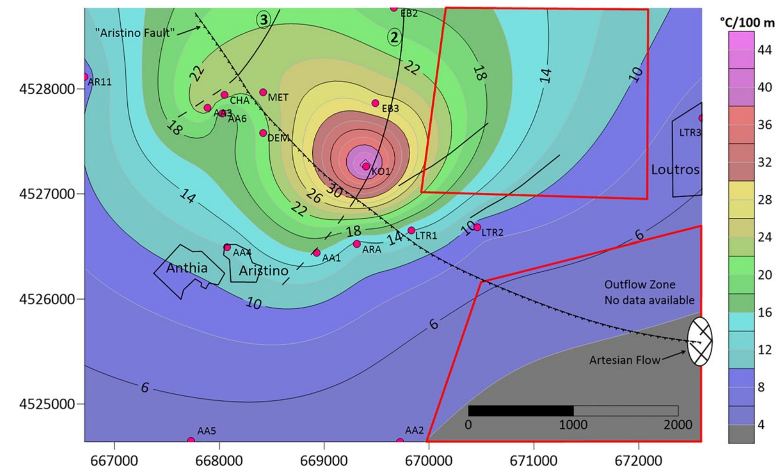

Fig. 16 Map of iso-gradient curves (°C/100 m), weighted by depth intervals. Red polygons show areas with interpolated values due to the absence of depth–temperature data

The plots b, c, d in Fig. 15 show the evolution of the mean thermal gradient in the most representative wells. The iso-gradient parts are associated with the presence of thick and homogeneous stratigraphic horizons. The significant variation of the calculated values, from 42 °C/km to over 450 °C/km, can be attributed to several causes, described in the following paragraphs.

Any increase or decrease observed in gradient profiles may account for a proportionate variation in the formation's thermal conductivity, an issue inadequately supported in this study, due to the lack of appropriate thermal conductivity measurements.

In Units B1 and B2, the thermal gradients exhibit drastic increase from south to north, which is related, apart from tectonics to the gradual thinning of the overlying sedimentary sequences up to their fully wedging out to the northernmost part of the study area.

The main mechanism accounted for heat transport in the upper system of the AGF is conduction. However, the observed gradient variations, in a relatively limited area, are much larger than those expected in a typical conductive system, where the thermal gradient changes are mainly or solely attributed to thermal conductivity. According to Estrada et al. (2001), if conduction was the dominant heat transfer mode, changes with position would occur less abruptly compared to a typical hydrothermal system, where heat transfer phenomena are mainly associated with the presence of faults, acting as water flow channels.

The different gradients and the high bottomhole temperatures in some wells are indicators of a critical and transitional regime between conduction (upwards) and convection (downwards). Apart from the cooler lowland and peripheral areas, the rest of the study area is likely to be strongly affected by nearby convective heat transfer, causing, in the most surficial parts, a strong vertical heat conduction component.

Since no obvious hydrothermal convection system can be deduced from the temperature–depth profiles, an overall conductive gradient was chosen as the average of straight-line segments, approximately weighted by depth interval. These values do not deviate significantly from the overall mean values, and hence, they are considered as the basis for the elaboration of the thermal gradient distribution map illustrated in Fig. 16.

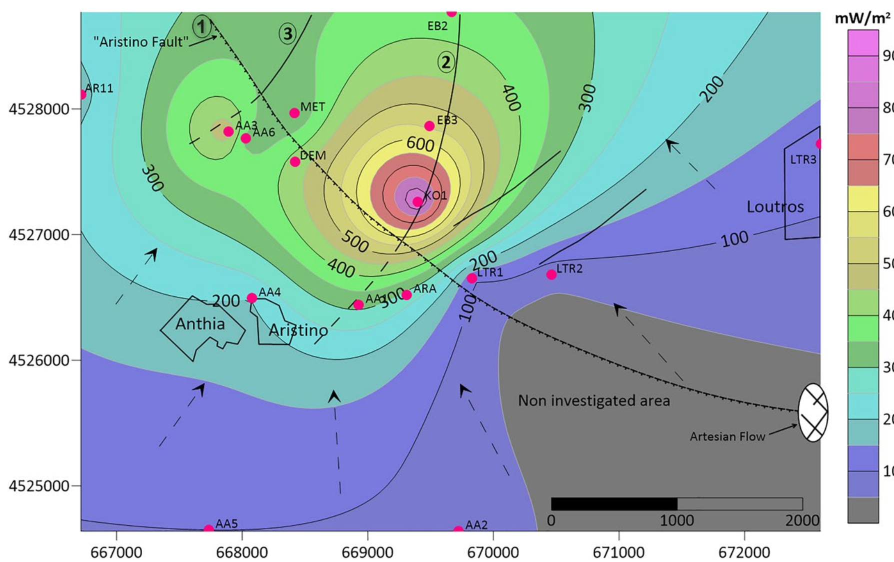

Fig. 17 Generalized heat flow map of the AGF. Dotted arrows depict the heat flow accumulation trend from the basin slags (SSW and SSE) to the marginal bulged/uplifted parts of the AGF

The thermal gradient varies significantly along a 10 km WNW–ESE axis, taking values almost 15 orders of magnitude higher than the mean value (32 °C/km) calculated in the deep oil well DEV-1.

Heat flow assessment

The mean heat flow values for the southern edge of the Evros basin range between 60 and 65 mW/m^2, as it was determined by Fytikas and Kolios (1979). According to Chiotis (1986), the geothermal gradient, based on data from the well DEV-1, is 32.6 °C/km and the heat flow at 61.6–65.5 mW/m^2, considering a mean thermal conductivity (K) at 1.89 W/m.K for the sedimentary sequences. The study of Tezcan and Turgay (1991) suggest heat flow values for the Greek part of Evros Delta Basin between 70 and 80 mW/m^2, assuming a constant thermal conductivity of $K = 2.1$ W/m.K.

Based on the above assumptions, a heat flow value of 65–70 mW/m^2 can be considered as the reference (mean) value for the southern, lower, and cooler part of the wider area (basin subsidence), which is close to the mean heat flow across all continents (Turcotte and Schubert 2002). All higher values referred in the present study are considered as anomalous.

For comparison purposes and based merely on the minimal values of thermal conductivities found in literature (Balkan et al. 2017; Dalla Santa et al. 2020) for identical rock formations, a weighted heat flow map for the AGF area is presented in Fig. 17.

The temperature survey and heat flow assumptions reveal a widespread circular positive anomaly, covering almost 15 km^2, inside the 200 mW/m^2 heat flow isoline. For values higher than 400 mW/m^2, heat flow converges in preferential accumulating zones, along the most known faults, in apexes parallel with temperature and thermal gradients. The area enclosed by the isoline of 400 mW/m^2 has an elliptical form, developing mainly toward the north, with its long axis coinciding with the trace of Fault 2 and bounded east and west by subparallel faults. The most significant heat flow accumulation is related to Fault 2, with values exceeding 800 mW/m^2 near to the intersection of Faults 1 and 2. A second "hot spot" semi-elliptical area is depicted in the out-bounding area, in the vicinity of the wells AA3 and AA6, adjacent to the intersection of Faults 1 and 3 (Fig. 17). The magnitude of the abnormal heat flow values is defined by the width and depth of the fractured zones, the presence or absence of significant cap rocks, and the location of the main deep feeding zones.

The whole area, around the elliptical hot spots and most specifically in the southern segments of the AGF, is characterized by the gradual increase of the isolines spacing, which is consistent with the increasing subsidence of the basin, the subsequent gradual decrease of thermal gradients, and the strong lateral thermal disturbances. Such a configuration corroborates the broad lateral conductive heat outflow to almost all directions, with different rates, depending on the faults activity and the lateral extent of the ignimbrites.

The lack of substantial data for the vertical development of the upper convection system in the ignimbrites and, most particularly, for the suspected deeper medium enthalpy hydrothermal system, limits the reliability of near-surface measurements of heat flow, as a basis for estimating the size of the heat resource and temperatures at depths greater than 500 m. In the case of AGF, the presumable widespread deep hydrothermal circulation plays an important role in the establishment of the most surficial conductive pattern, largely affecting the magnitude and distribution of the heat flow.

According to Gokturkler et al. (2003) who have numerically processed the conductive heat transfer in Western Anatolia (Turkey), hydrothermal circulation might produce high near-surface heat flow, which may not represent the deeper heat flow and main values of the region. In the Roosevelt Hot Springs (USA) high temperature geothermal system, the heat loss (by conduction) to the surface is significant, despite the insubstantial fluid discharge. In this case, the center of the system is delineated by the 1000 mW/m^2 (ten times background) contour. The heat loss in excess was attributed to the proximity of the main reservoir to the surface (Chapman and Rybach 1985).

The conceptual model of Aristino-Traianoupolis geothermal area

A conceptual 3D model of the thermal regime in the wider AGF area is presented in Fig. 18, taking into consideration the corrected temperatures (max. 140 °C) at various depths in the oil well DEV1 and the measured static ones to a maximum depth of 500 m**.** The mean thermal gradient distribution has also been incorporated. The plotting of isotherms up to 100 °C is more reliable, whereas those of 120 °C and 140 °C were drawn arbitrarily, based merely on the extrapolated conductive profiles of the wells examined (Fig. 12d). The temperature distribution pattern is consistent with the steep subsidence of the wider area, from the uplifted, low-mountainous margins of the basin to the deepest parts filled with almost 3200 m of low conductivity sedimentary rocks.

The densification of isotherms in the form of a localized thermal plume coincides with the location of the investigated geothermal field. This bell-shaped thermal anomaly is bounded to the south by the local base reference thermal gradient value of 40 °C/km (wells AA5 and AA2). Southeastwards, the drop of isotherms is getting sharper, following the increasing rate of the basement down slip and the decreasing heat flow rates,

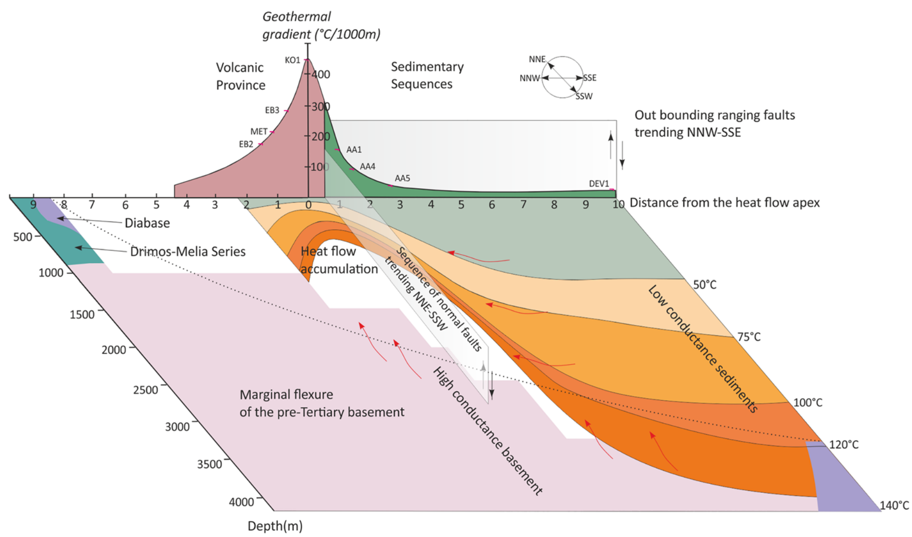

Fig. 18 Temperature distribution in a 3D conceptual model of the Aristino-Traianoupolis geothermal area

induced by the increasing thickness of the low conductivity sediments. The basement down slip can be deduced by the occurrence of the CRB diabases. Such Cretaceous diabases (dolerites and spilites) outcrop at the margins of the basin, 8–10 km north of the main geothermal anomaly (Papadopoulos 1980), at altitudes of 200–300 m. In the southern edge of the basin, 10 km SE of the main geothermal anomaly, metadiabases have been penetrated by the deep oil well DEV1 at 3270 m depth (Sousounis 1993).

The emplacement of the AGF at the bulged/uplifted SSW margins of the Evros Delta sub-basin may explain some of the thermal characteristics discussed in this paper, as, for example, the "basement edge effects," which, as described by Huvaz et al. (2007), Wang et al. (2020), and Yu et al. (1995), is likely to be associated with high heat fluxes, triggering heat to be retained in conductive (basement) rocks and giving rise to heat flow anomalies at the edges of a graben or in steeply dipping margins of a basin.

Results and discussion

The wider Aetochori-Aristino-Loutros area is located at the southwestern bulged/uplifted margins of the Thrace basin and has been affected by intense hydrothermal activity. The elevated heat flow, for the deeper parts of the Evros Delta sub-basin, has affected an area over 50 km^2, giving rise to a substantial regional geothermal anomaly, which is driven by a series of interrelated factors as discussed here and set out in the previous chapters.

The actual thermal regime in the AGF area reflects the active traces of the fossil widespread Oligocene to Miocene thermal culmination and hydrothermal circulation that affected the entire volcanic and volcaniclastic province, witnessed by the presence of the widespread hydrothermal alteration assemblages and mineral zoning (silicic, argillic, sericitic, and propylitic zones) with polymetallic mineralization (Au, Ag, Zn, Pb, Cu, and Mo) (Marantos et al. 2007).

The local high thermal anomaly is restricted in a relatively narrow area comprising the volcanic highlands (bulges) and volcano-sedimentary lowlands (sags) bounded and segregated by active bordering deep oblique-slip faults striking NNW–SSE and NNE–SSW, respectively. Recently recognized buried E–W striking faults are also likely to play a critical role. Both dominating fault groups evolve in the form of parallel or subparallel successions, causing the progressive subsidence of the area toward the SW and SE in a half rift configuration, characteristic of a basin uplifted marginal area.

The AGF area does not exhibit any substantial surficial fluid discharge, apart from the low-rate artesian well drilled in the Traianoupolis thermal center area. This "blind geothermal system" is characterized by fracture-controlled permeability, preferentially along the most active damage-fault zones and the intersection of faults or fault blocks. Secondary permeability plays the most critical role to the establishment of deeper hydrothermal convection systems and upwelling pathways. The widespread lateral heat transfer through interlayered hot aquifers is closely associated with the main structural channels. The lateral water movement is more conspicuous in the case of the ignimbrite (upper geothermal system), emplaced in a longitudinal band covering almost 5 km^2, an issue supported by the similar hydrochemical characteristics of water samples and the widespread elevated subsurface temperatures measured in scattered boreholes tapping the ignimbrite.

The distribution of temperatures for values higher than 50 °C is represented by a quasi-circular thermal anomaly covering almost 8 km^2 with focalized increments associated with structural effects. The maximum water temperature of 99 °C was measured during a pumping test, while maximum static bottomhole temperatures of 92.5 °C and 90 °C were measured in the volcanic and volcano-sedimentary units, respectively. The lateral variation of the thermal gradient is significant throughout a relatively limited zone and ranges from 42 °C/km to more than 400 °C/km, whereas it shows a general trend to decrease with depth. The heat flow, even for low thermal conductivities, shows a great range of values from 80 mW/m^2 to more than 800 mW/m^2. The thermal profiles of static temperatures at depths as great as 250 m in the volcanic and 500 m in the volcano-sedimentary sequences are characterized by constant increase of temperature. They do not exhibit any substantial disturbance by cooler inflows from peripheral groundwater, except in the southern lowlands. So far there is no significant and systematic heat extraction or natural water discharge from the AGF. Consequently, all temperatures presented in this study are considered as representative of thermal equilibrium regarding the penetrated formations.

Given the abnormally high values of the three key thermal parameters (temperature, thermal gradient, and heat flow) even for very low depths, as well as the sharp transitional effects, any attempt to interpret the thermal patterning only through conduction should require unrealistic variations in thermal conductivity between lithostratigraphic units. According to Estrada et al. (2001), when an area is dominated by conduction, processes governing transitional heat transfer occur much more progressively than in a hydrothermal convection-dominated system, where governing heat transfer phenomena change with position much more sharply.

All thermal features regarding most surficial parts of the AGF agree with the aforementioned approach and support the hypothesis for the presence of a well-focalized convective hydrothermal system established within overlapping reservoirs, separated by impermeable strata at depths greater than those investigated up to now. Target

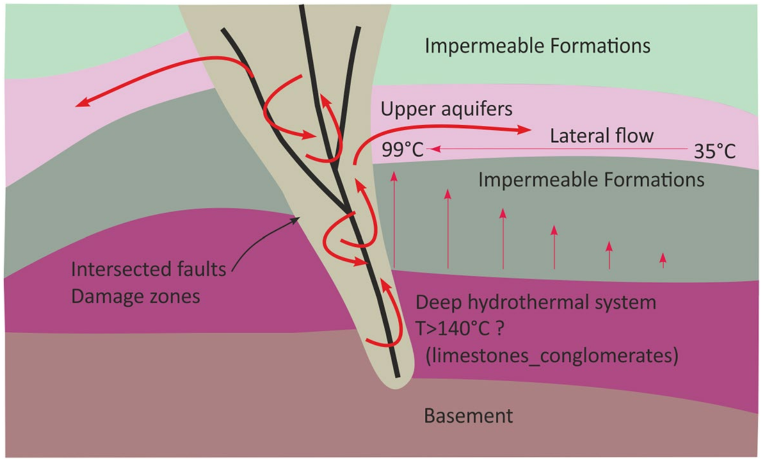

Fig. 19 Generalized geological sketch (not to scale) and conceptualization of the dominant heat transfer process in the AGF. The water movement is conducted through permeable intersected faults damage zones and permeable overlapping lateral reservoirs (modified from Liotta et al. 2021)

depths to the hottest parts of the AGF seem to follow the general trend of gradual increase from the heat accumulation apex in the tectonized volcanics to the subsidized and cooler volcano-sedimentary units to the south.

Convection evolves mostly vertically, in the form of upwelling, well-directed heat intrusions alongside active damage zones, triggered by deep-slip normal faults and most surficial fractures, as it is clearly illustrated in Fig. 7 by the shape of the low resistivity zones.

The upwelling fractured zones form an interrelated multi-directional thermal network, which affects laterally the entire area, causing a generalized thermal anomaly, where vertical movement of hot fluids is combined with a broad lateral leakage to almost all directions, with variable intensity.

With reference to the distinction between geothermal systems, proposed by Liotta et al. (2021), the presumed convection dominated system constitutes a fault leakage-controlled structure, where high temperature fluids move from the deeper hydrothermal system into the fault damage zones, followed by fluid leakage into more surficial lateral permeable and concealed layers (Fig. 19). These layers may cover large areas that extend beyond the feeding-damage zones, at distances of some kilometers. The temperature of the laterally moving fluids undergoes horizontal variations because of the gradually changing magnitude of the heat flow.

The Aristino-Traianoupolis geothermal area is an interesting case study that offers the possibility to correlate the distribution patterns of measured temperatures with the localization of heat intrusions, which have been mapped as zones of very low electrical resistivity. These zones are spatially represented as 2D and/or 3D interrelated views at maximum depths of 500 m (personal communication with P. Tsourlos and G. Vargemezis). They are in good agreement with the known active fractured zones (conductive structures), the lithology, and localization of the hot aquifers described in the present study as upper geothermal system.

The overall scientific approach for the identification and characterization of the thermal properties and driving mechanisms of this system was based on temperature data acquired during the last 25 years and the conceptualization of the thermal regime. The observed thermal pattern postulates the direct involvement of deeper and hotter hydrothermal systems, the presence of which is of utmost importance for the establishment of the upper, thoroughly investigated, geothermal system. In this direction, a future, more elaborated, application of electromagnetic geophysical methods would be of crucial interest for detecting the amplitude and penetrating depth of the investigated most surficial conductive structures.

The presence of deeper systems is further supported by the deep equilibration temperature values, estimated from chemical and isotopic geothermometers. Chemical geothermometers were first applied by Poutoukis and Dotsika (1998) on water samples from the KO1, EB3 wells, and the Traianoupolis thermal spring, suggesting deep equilibration temperatures in the order of 140–150 °C. Recently, chemical (SiO_2, Li–Mg, Na–K, Na–Li and Na–K–Ca) and isotopic [$\delta^{18}O$–(H_2O–SO_4)] geothermometers were applied on water samples from the majority of the investigated wells and the Traianoupolis thermal spring (Dotsika et al. 2021). The resulting temperatures vary among the applied geothermometers, mainly disturbed by the contribution of marine solutions to the deep thermal fluids. Due to the oversaturation of the waters in silica (>0.8) and considering that the silica geothermometer is not affected by marine involvement in the deep reservoir and the temperature range (94–130 °C) obtained by this geothermometer may be considered as representative of the lowest accepted values attributable to the deepest thermal waters. The maximum temperatures (170–200 °C and 150–190°), estimated by the Na–K and Na–K–Ca and the sulfate-water isotopic geothermometers, respectively, provide evidence for the presence of a medium enthalpy deep hydrothermal system.

In any case, the thermal response of the AA6 well indicates that temperatures higher than the maximum measured ones (90–99 °C) should be expected even for the upper system (as presented in Table 1).

The non-aggressive thermal fluids with temperatures from 60 to 99 °C that are found at very low depths, account for a reliable and potentially profitable local energy resource, which has not been exploited so far; nevertheless, an important pilot project implemented by the Municipality of Alexandroupolis is currently at its final stage, regarding space/district heating and agricultural use of geothermal energy (Papachristou et al. 2020). The (on-going) geothermal exploration and the acquired scientific knowledge correspond satisfactorily to the objectives of the upper geothermal system exploitation project.

On the other hand, the investigation and exploitation of the still probable, deeper, reservoirs constitute a major challenge not only for the specific geothermal field but also for other geothermal areas, especially in Northern Greece. To that end, the systematic review, analysis, evaluation, and interpretation of all the available data for the AGF could establish an evidence-based qualitative and partially quantitative approach, applicable to similar cases, where potential medium enthalpy resources are obviously still unconfirmed.

Abbreviations

AGF Aristino geothermal field
CRB Circum-Rhodope belt
TEM Transient electromagnetic method
ERT Electrical resistivity tomography
bmsl Bellow mean sea level

Acknowledgements

The authors gratefully acknowledge Andreas Ilias for its continuous and timeless assistance in field work and acquisition of pumping tests and borehole monitoring data. They also thank Nikos Kolios for fruitful discussions and constructive comments. They thank Panagiotis Tsourlos and George Vargemezis for sharing unpublished data concerning Electrical Resistivity Tomographies. They would like to express their sincere appreciation to the Municipality of Alexandroupolis for the ongoing support, technical and scientific collaboration with the Institute of the first author since 2012. More particularly, they would like to address their gratitude to the former Deputy Mayor of Alexandroupolis Giannis Falekas, who warmly embraced their work and fully supported the development of the Aristino geothermal field. A. Panagopoulos is also thanked for his constructive comments. Moreover, they would like to thank the Anonymous Reviewers and the Editor for their time and effort to review and improve the manuscript.

Author contributions

PD, the corresponding author, contributed to conceptualization, writing—original draft, field work, data acquisition and processing, visualization, validation, and supervision. MP was involved in methodology, writing—review and editing, and supervision. PN contributed to writing—review and editing, and methodology.

Funding

The first author acknowledges partial funding from the Municipality of Alexandroupolis through a long standing technical and scientific collaboration in the frame of the Aristino geothermal field exploration project.

Availability of data and materials

The datasets analyzed during this study are available from the corresponding author on reasonable request.

Declarations

Competing interests

The authors declare that they have no known competing financial interests or personal relationships that could have appeared to influence the work reported in this paper.

Received: 8 March 2022 Accepted: 15 September 2022
Published online: 01 October 2022

References

Arikas K, Voudouris P. Hydrothermal alterations and mineralizations of magmatic rocks in the southeastern Rhodope massif. Acta Vulcanol. 1998;10(2):353–65.

Attri A, Zuffa G, Cavazza W, Okay A, Di Vincenzo G. Detrital supply from subduction/accretion complexes to the eocene-oligocene post-collisional southern thrace basin (NW Turkey and NE Greece). Sed Geol. 2012;243:117–29. https://doi.org/10.1016/j.sedgeo.2011.10.008.

Balkan A, Erkan K, Salk M. Thermal conductivity of major rock types in western and central anatolia regions Turkey. J Geophys Eng. 2017;14:909–19. https://doi.org/10.1088/1742-2140/aa5831.

Caracciolo L, Orlando A, Critelli S, Kolios N, Manetti P, Marchev P. The tertiary thrace basins of SE Bulgaria and NE Greece: A review of petrological and mineralogical data of sedimentary sequences. Acta Vulcanol. 2015;25:21–41.

Chapman D, Rybach L. Heat flow anomalies and their interpretation. J Geodyn. 1985;4:3–37.

Chiotis E. 1986 Evaluation of corrected temperatures measurements and heat flow estimation at deep oil wells in Greece. Proceedings of the 3rd Congress of the Geological Society of Greece. 20(3); 197–215

Christodoulou G. Über das alter einiger formationen von samothraki (in Greek with German summary). Bull Geol Soc Greece. 1958;3(1):40–5.

Christofides G, Pecskay Z, Elefteriadis G, Soldatos T, Koroneos A. The tertiary evros volcanic rocks (Thrace, Northeastern Greece): petrology and K/Ar geochronology. Geol Carpath. 2004;55:397–409.

Dalampakis P, Spyridonos E, Tassi M, Karalis P, Dotsika E, Pagonis G. Chemical and Isotopic Characterization of the thermal fluids in the south-western margin of the Loutros-Feres-Soufli Tertiary Basin in Northern Greece. Case Study: Geothermal Area of Aristino. 17th International Conference on Environmental Science and Technology, Athens, Greece; 2021.

Dalla Santa G, Galgaro A, Sassi R, Cultrera M, Scotton P, Mueller J, Bertermann D, Mendrinos D, Pasquali R, Perego R, Pera S, Di Sipio E, Cassiani G, De Carli M, Bernardi A. An updated ground thermal properties database for GSHP applications. Geothermics. 2020;85(101758):1–13. https://doi.org/10.1016/j.geothermics.2019.101758.

Dimadis E, Nikolov T. An ammonite find in the makri unit (Berriasian, Southeast Rhodopes, Northeast Greece). C R Acad Bulg Sci. 1997;50:71–4.

Dotsika E, Dalampakis P, Spyridonos E, Diamantopoulos G, Karalis P, Tassi M, Raco B, Arvanitis A, Kolios N, Michelot JL. Chemical and isotopic characterization of the thermal fluids emerging along the North-Northeastern Greece. Sci Rep. 2021;11(16291):1–12. https://doi.org/10.1038/s41598-021-95656-6.

Estrada G, Hernandez A, Ledesma R. Temperature-depth relationships based on log data from the los azufres geothermal field Mexico. Geothermics. 2001;30:111–32.
Fytikas M, Kolios N. Preliminary heat flow map of Greece. In: Cermat V, Rybach L, editors. Terrestrial heat flow in Europe. Springer Verlag; 1979. p. 197–205.
Gokturkler G, Salk M, Sari C. Numerical modeling of the conductive heat transfer in western anatolia. J Balkan Geophys Soc. 2003;6(1):1–15.
Huvaz O, Karahanoglou N, Ediger V. The thermal gradient history of the Thrace basin, NW Turkey: correlation with basin evolution processes. J Pet Geol. 2007;30(1):3–24.
Innocenti F, Kolios N, Manetti P, Pecerillo G, Rita F, Villari L. Evolution and geodynamic significance of the tertiary orogenic volcanism in Northeastern Greece. Bull Volcanol. 1984;47(1):25–37.
Karmis P, Vargemezis G, Papadopoulos I, Tsourlos P. The application of the transient EM method into the geothermal field exploration. Bull Geol Soc Greec. 2004;36:1224–33.
Kilias AD, Vamvaka A, Falalakis G, Sfeikos A, Papadimitriou E, Gkarlaouni CH, Karakostas B. The mesohellenic trough and the paleogene thrace basin on the Rhodope massif, their structural evolution and geotectonic significance in the hellenides. J Geol Geosci. 2015;4:2. https://doi.org/10.4172/2329-6755.1000198.
Kolios N. Geothermal exploration in the Aristino-Antheia area (Prefecture of Evros). Thessaloniki: Technical and scientific report IGME; 2001.
Kolios N, Fytikas M, Arvanitis A, Andritsos N, Koutsinos S. Proceedings European Geothermal Congress. Germany: Unterhaching; 2007. p. 1–11.
Kolios N, Koutsinos S, Arvanitis A, Karydakis G. Geothermal situation in Northern Greece. Proceedings World Geothermal Congress Antalya Turkey. 2005
Kopp KO. Geologie Thrakiens III : Das Tertiaer zwischen Rhodope und Evros Ann Géol. Pays Hellénique. 1965;16:315–62.
Liotta D, Brogi A, Ruggieri G, Zucchi M. Fossil vs active geothermal systems a field and laboratory method to disclose the relationships between geothermal fluid flow and geological structures at depth. Energ. 2021;14(933):1–26. https://doi.org/10.3390/en14040933.
Magganas A, Sideris C, Kokkinakis A. Marginal basin-volcanic arc origin of metabasic rocks from the Circum-Rhodope Belt, Thrace Greece. Mineral Petrolog. 1991;44:235–52.
Marantos I, Markopoulos T, Christidis E. Zeolitic alteration in the tertiary feres volcano-sedimentary basin, Thrace NE Greece. Mineral Magazin. 2007;7(3):327–45. https://doi.org/10.1180/minmag.2007.071.3.327.
Marantos I. 2004 Study of the Tertiary volcanic rocks alteration in the Feres basin of Evros prefecture, emphasizing on the genesis of zeolites and their possible applications. PhD thesis, Technical University of Crete, Department of Mineral Research Engineering, Chania, Greece
Marchev P, Kaiser-Rohrmeier M, Heinrich C, Ovtcharova M, von Quadt A, Raicheva R. 2: Hydrothermal ore deposits related to post-orogenic extensional magmatism and core complex formation: the Rhodope Massif of Bulgaria and Greece. Ore Geol Rev. 2005;27(1–4):53–89. https://doi.org/10.1016/j.oregeorev.2005.07.027.
Meinhold G, BouDagher-Fadel MK. Geochemistry and biostratigraphy of Eocene sediments from Samothraki Island, NE Greece. N Jb Geol Palaeont Abh. 2010;256(1):17–38. https://doi.org/10.1127/0077-7749/2009/0031.
Michael C, Katirtzoglou C, Perdikatsis V, Constantinides D. The polymetallic mineralization of the pefka area, evros county Greece. Geolog Rhodopica. 1989;1:322–9.
Papachristou M, Dalampakis P, Arvanitis A, Mendrinos D, Andritsos N. 2020 Geothermal developments in Greece—Country update 2015–2020. Proceedings World Geothermal Congress, Reykjavik, Iceland
Papadopoulos P, Arvanitides ND, Zanas I. Some preliminary geological aspects on the makri unit (phyllite series): peri-Rhodopian zone. Geol Rhodopica. 1989;1:34–42.
Papadopoulos P. Geological map of Greece, Ferai – Peplos - Ainos sheet, scale 1:50 .000. IGME, Athens. 1980.
Piscopo V, Formica F, Lana L, Lotti F, Pianese L, Trifuoggi M. Relationship between aquifer pumping response and quality of water extracted from wells in an active hydrothermal system: the case of the island of Ischia (Southern Italy). Water. 2020;12:2576. https://doi.org/10.3390/w12092576.
Plougarlis A, Tranos M. Geology of ammouliani island (Northern Greece)—implications for the tectono-magmatic evolution of the serbo-macedonian massif. J Maps. 2015;11(4):552–60. https://doi.org/10.1080/17445647.2014.948504.
Poutoukis D, Dotsika E. Contribution of isotope hydrology and hydrogeochemistry in the study of the geothermal field of aristino area evros. proceedings of the 8th international congress, patras,. Bull Geol Soc of Greece. 1998;4:69–79.
Rondoyanni T, Georgiou C, Galanakis D, Kourouzidis M. Evidences of active faulting in Thrace region (North-Eastern Greece) proceedings of the 10th international congress. Bull Geol Soc of Greece. 2004;36(4):1671–8.
Sousounis G. Estimation of the hot dry rocks (HDR) with data from boreholes and seismic data. 2nd Congress of the Hellenic Geophysical Union, Florina, Greece. 1993;2:276–87.
Tezcan AK, Turgay MI. Heat flow and temperature distributions in Turkey. In: Cermak V, Haenal R, Zui V, editors. Geothermal Atlas of Europe: Herman HAACK Verlag. Germany: Gotha; 1991.
Tranos MD. Faulting of lemnos island; a mirror of faulting of the north aegean trough (Northern Greece). Tectonophys. 2009;467:72–88. https://doi.org/10.1016/j.tecto.2008.12.018.
Tranos MD. Strymon and strymonikos gulf basins (Northern Greece): implications on their formation and evolution from faulting. J Geodyn. 2011;51:285–305. https://doi.org/10.1016/j.jog.2010.10.002.
Tranos M. D. Contribution to the study of the neotectonic deformation in the region of Central Macedonia and North Aegean. PhD thesis, University of Thessaloniki. 1998.
Turan A, Saner S, Artun E. Intersecting fracture geometries in control of geothermal spring occurrences in circumferences of the madra mountain aegean region of Turkey. GRC Trans. 2016;40:611–9.
Turcotte DL, Schubert G. Geodynamics. 2nd ed. Cambridge: Cambridge University Press; 2002. p. 456.
von Braun E. The Rhodope question viewed from eastern greece. Zeitschrift Der Deutschen Geologischen Gesellschaft. 1993;144:406–18.

Wang X, Mao X, Mao X, Kewen L. Characteristics and classification of the geothermal gradient in the Beijing–Tianjin–Hebei Plain China. Math Geosci. 2020;52:783–800. https://doi.org/10.1007/s11004-019-09814-8.
Yu Z, Thomsen RO, Lerche I. Crystalline basement focusing of heat versus fluid flow/compaction effects: a case study of the I-1 well in the danish north sea. Petroleum Geosci. 1995;1(1):31–5.

Publisher's Note